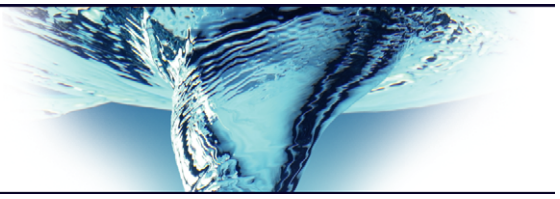
*J. Fluid Mech.* (2013), *vol.* 733, R3, doi:10.1017/jfm.2013.456

JFM RAPIDS
journals.cambridge.org/rapids



# Nucleating bubble clouds with a pair of laser-induced shocks and bubbles

**Pedro A. Quinto-Su**[1],† **and Keita Ando**[2]

[1]Instituto de Ciencias Nucleares, Universidad Nacional Autónoma de México, Apartado Postal 70-543, 04510 México D.F., Mexico

[2]Department of Mechanical Engineering, Keio University, Yokohama 223-8522, Japan

(Received 22 July 2013; revised 28 August 2013; accepted 29 August 2013; first published online 23 September 2013)

Laser-induced optical breakdown at two spatial locations in ultrapure water saturated with ambient gas is used to nucleate microscopic bubble clouds with lifetimes of tens of nanoseconds. The liquid is ruptured via the interaction of a pair of laser-induced shocks and bubbles. We find that the acoustically nucleated micro-bubbles appear in a localized region defined by the plane that bisects the pair of foci, where rarefaction waves (reflected from the laser-induced bubbles) merge. We measure the probability for acoustic nucleation as a function of the separation between the foci, and the minimum pressures for each separation are calculated with Euler flow simulations. The simulations show that the liquid is exposed to negative pressures for 3–17 ns. A statistical threshold pressure for cavitation inception (0.5 probability) of $-20.1 \pm 3.4$ MPa is extracted from the measured probabilities and the calculated minimum pressures.

**Key words:** bubble dynamics, cavitation, shock waves

## 1. Introduction

Shock–bubble interaction is a classical fluid dynamics problem (Ohl & Ohl 2013) that incorporates many physical phenomena such as shock transmission and/or reflection, adiabatic compression of bubble contents, shape instabilities, non-spherical bubble collapse with jetting and vorticity generation (Haas & Sturtevant 1987; Layes, Jourdan & Houas 2003; Ranjan, Oakley & Bonazza 2011).

In the problem of shock–bubble interaction, shocks reflect at bubble walls as tension waves (negative pressure) due to acoustic impedance mismatch (Leighton 1994). As a result, the liquid is stretched. In principle, the reflected tension may rupture the liquid, nucleating cavitation bubbles if the tension overcomes the tensile strength of the liquid. However, previous studies have not observed cavitation as a result

† Email address for correspondence: pedro.quinto@nucleares.unam.mx

© Cambridge University Press 2013



https://doi.org/10.1017/jfm.2013.456 Published online by Cambridge University Press

of shock–bubble interaction, probably because the reflected waves are geometrically defocused; thus their amplitudes are not strong enough to rupture the liquid. Cavitation bubble nucleation due to ultrasound–bubble interaction has been reported in the recent work of Maxwell *et al.* (2011), which observed cavitation clouds arising from the backscattering of focused ultrasound bursts on cavitation bubbles formed during the initial cycle of the acoustic pulse. The observations were explained by constructive interference between the reflected negative pressure and the negative pressure phase of the ultrasound burst.

In this work we explore cavitation bubble cloud nucleation induced by the interaction of a pair of laser-induced shocks and bubbles in water. The spatial configuration of the laser pulse is the same as that used in studies of non-spherical bubble collapse with jetting (Quinto-Su & Ohl 2009; Ohl & Ohl 2013) and in applications with biological cells (Sankin, Yuan & Zhong 2010; Jayasinghe, Rohner & Hutson 2011) and carbon nanotubes (Quinto-Su *et al.* 2010). Here the key idea is the superposition of a pair of tension waves (resulting from shock–bubble interactions) that stretch the liquid in a time scale of nanoseconds.

In the following sections we describe the experimental set-up, the experiment, the numerical model used to simulate the pair of bubbles and shocks, results on the probability of nucleation, and finally we compare our results with other acoustic experiments.

## 2. Experimental set-up

The experimental set-up is shown in figure 1. Single pulses from a frequency-doubled Nd:YAG laser (laser 1; New Wave, Orion) are used to create breakdown in water at two locations; the laser pulses have a duration of 6 ns and a wavelength of 532 nm. The polarization of the beam (linear) is rotated with a half-wave plate, and then it is expanded with a telescope (not shown) in order to overfill the screen of a spatial light modulator (SLM; Holoeye LC-R 2500). The SLM is a diffractive element that is used to shape the beam in order to focus simultaneously at different spatial locations. The polarizations of the incident and reflected beams are set to get a mainly phase modulation. The digital holograms projected onto the SLM are calculated with a simple Gerchberg–Saxton algorithm (Gerchberg & Saxton 1972). The pulse reflects at the SLM and propagates through lens L1, which projects the desired bifocal pattern at the focal plane located at a distance $f_1$ from the lens ($f_1 = 400$ mm). A spatial filter is used to remove the zero undiffracted order and the unwanted higher orders. Lens L2 ($f_2 = 100$ mm) recollimates the beam; the polarization is set with a half-wave plate and polarizing beam splitter (PBS) cube. Lenses L3 ($f_3 = 200$ mm) and L4 ($f_4 = 250$ mm) change the size of the beam to match the diameter of the back aperture of the microscope objective. The beam is coupled to an inverted microscope (Olympus IX-71) with a dichroic mirror that reflects the wavelength of the laser into the back aperture of the microscope objective (40×, 0.8 NA, WD 2.5 mm water immersion). The bifocal beam pattern is projected by the microscope objective inside the liquid far away from any boundaries (1.5 mm from the bottom coverslip) in the plane $z = 0$ (figure 1, inset).

A second frequency-doubled Nd:YAG laser (laser 2; New Wave, Solo PIV) is used for strobe illumination to capture the dynamics of the events. The beam is focused into a dye cell (Exciton Rhodamine 698 diluted in methanol) to excite emission centred at 698 nm. The emitted 698 nm pulses are coupled to an optical fibre that directs the light into the condenser of the microscope to illuminate the sample with a time



https://doi.org/10.1017/jfm.2013.456 Published online by Cambridge University Press

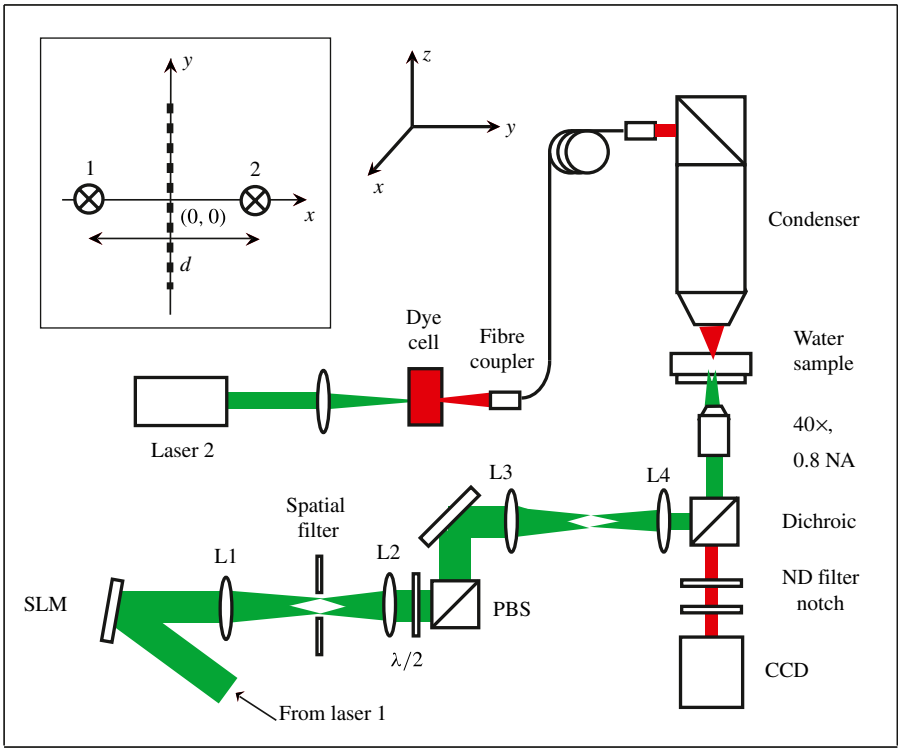



FIGURE 1. Experimental set-up. Inset: geometry of the bifocal array where optical breakdown is achieved. The laser is simultaneously focused at two locations of the *xy* plane represented by the numbered cross-hairs. The bisecting plane is represented by the dashed line.

resolution of ±2.4 ns (half-width at half-maximum). The events are imaged by the microscope objective with submicrometre spatial resolution and are recorded by a charge-coupled device (CCD) camera (Sensicam QE). A pulse generator controls the timing between the two lasers. The combined jitter considering the arrival of the laser pulses into the sample and the time when the plasma reaches its maximum size is ±0.7 ns. Hence the uncertainty in time is ±3.1 ns. A neutral density filter and a notch filter are placed in front of the CCD to avoid saturation. A Petri dish with a no. 1 coverslip (0.13–0.16 mm thick) at the bottom is filled with 3 ml of ultrapure water at room temperature (Millipore, 18.2 MΩ cm), and then it is covered and placed on the inverted microscope stage. The images are taken in the plane $z = 0$ (figure 1, inset) and did not capture any visible-sized impurities such as small particles or gas bubbles within the water.

## 3. Experiment

The geometry of the bifocal array where optical breakdown is achieved is shown in the inset of figure 1. The numbered cross-hairs represent the two spatial locations (in the plane defined by $z = 0$) where a single laser pulse is simultaneously focused, while the dashed line represents the bisecting or contact plane between the pair of foci where shocks and tensions overlap. The experiments were done for eight different separations between the foci: $d = 50.9,\ 58.8,\ 66.5,\ 74.4,\ 82.1,\ 90.1,\ 97.9,\ 105.8 \pm 0.6$ μm. The



https://doi.org/10.1017/jfm.2013.456 Published online by Cambridge University Press

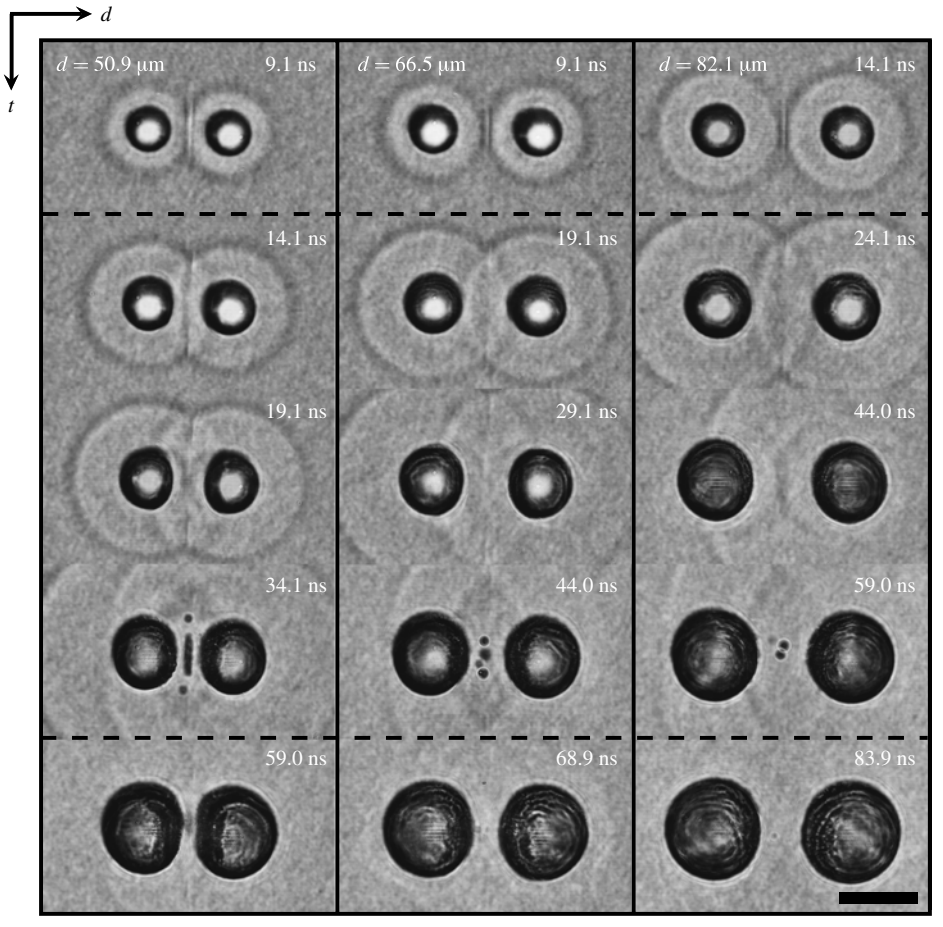



FIGURE 2. Dynamics of bubbles and shock waves induced by optical breakdown at two foci separated by (left to right) $d = 50.9$, 66.5 and 82.1 μm. The length of the scale bar is 50 μm and the energy at each focus is 72.5 μJ.

mean energy at each focal volume is 72.5 μJ, with a variation of 5 % for all the separations. Hence we essentially have identical plasmas at all the separations. At each focal volume, the plasma expands during the absorption of the laser pulse to a maximum transverse radius (luminescent area) between 7 and 9.4 μm. The dynamics of the induced shocks and expanding vapour bubbles are imaged for delays in the range between 4 and 90 ns after the arrival of the laser pulse. For each time delay and separation, the experiment is repeated five times. All the experiments are repeated at a constant rate every 5 s.

Figure 2 shows the dynamics of the pair of shock waves and bubbles induced by systems of two plasmas. Each column shows the evolution of the system for a particular separation (left to right: 50.9, 66.5, 82.1 μm), with the earliest time at the top. The first row in figure 2 shows the initial overlap of the shock waves at the bisecting or contact plane ($yz$ at $x = 0$), which can be observed on the images as a straight segment due to the sudden pressure and refractive index change. As both shock fronts expand, the shock waves keep colliding at the contact plane but with



https://doi.org/10.1017/jfm.2013.456 Published online by Cambridge University Press

lower pressures. The images in the second row are taken at times when the shock fronts are reaching the surfaces of the opposing laser-induced bubbles. Images in the third row show the reflected tensions overlapping at the contact plane causing an abrupt drop in the pressure. We find bubble nucleation, whose probability depends on $d$, a few nanoseconds after the tensions overlap, since it takes such a waiting time for the nucleated nanobubbles to expand to a size of a few hundred nanometres that can be resolved by the imaging system (fourth row of figure 2). We observe that the bubble clouds are mainly nucleated along a small region of the contact or bisecting plane centred at the origin. Hence, the clouds have a shape similar to a line segment or a cigar ($xy$ plane), which is really a disk because of the axial symmetry of the system. The length of the nucleated clouds decreases with increasing $d$. At even larger separations, it is more common to just nucleate a single submicrometre bubble. Later, the tensions reflect again at the laser-induced bubbles as compressions that can collapse the nucleated bubbles (last row of figure 2). At this stage, instabilities at the surface of the bubbles can be observed and possibly bubble nucleation.

## 4. Simulation

An axisymmetric Euler flow solver (Johnsen & Colonius 2006, 2009; Ando, Liu & Ohl 2012) is used to simulate the two-plasma system; the laser-induced bubbles are treated as ideal gases (non-condensible), used to model the rapid expansion of the plasma – see the supplementary material (available at http://dx.doi.org/10.1017/jfm.2013.456) for details of physical and numerical modelling. The initial conditions for the individual plasmas (radius and pressure) are extracted from another set of experiments (with the same conditions as the ones shown in figure 2) where one focused laser spot is blocked to get the individual dynamics of a single laser-induced shock and bubble. The dynamics are essentially the same for all the separations. The (numerically well converged) solution with initial plasma conditions of radius $R_0 = 8$ μm and pressure $P_i = 2$ GPa (continuous lines on figure 4$a$) yields a reasonable fit for the dynamics of the laser-induced bubble and shock wave within the uncertainties of the experiment. The initial plasma radius $R_0$ in the simulation is consistent with the measured effective radius of the expanded luminescent plasma (7–9.4 μm). Hence the simulation starts ($t = 0$) when the plasma has reached the maximum size. Figure 3 shows the simulated Schlieren images for the cases shown in figure 2 between the dashed lines for plasmas with an initial radius of $R_0 = 8$ μm and initial pressure $P_i = 2$ GPa. The simulations of the two-plasma system capture the imaged dynamics, including the shapes of the bubbles and the evolution of the pressure waves (see supplementary material). The individual dynamics of the laser-induced shock and bubble are plotted in figure 4($a$), where each data point represents the average of all the data for that particular time delay, that is, 80 events (left, right, eight distances, five repetitions each).

## 5. Results and analysis

The probability for microscopic bubble cloud nucleation is measured for the eight different separations $d$. The probability is judged based on whether nucleated bubbles (submicrometre) are observed or not. For each separation we look at 118–135 events. Observations are made a few nanoseconds after the tensions overlap and before the tensions reflect again as positive pressures. Hence, most observations are made after a single cycle of negative pressure (except for $d = 82.1$ μm according to simulation).



https://doi.org/10.1017/jfm.2013.456 Published online by Cambridge University Press

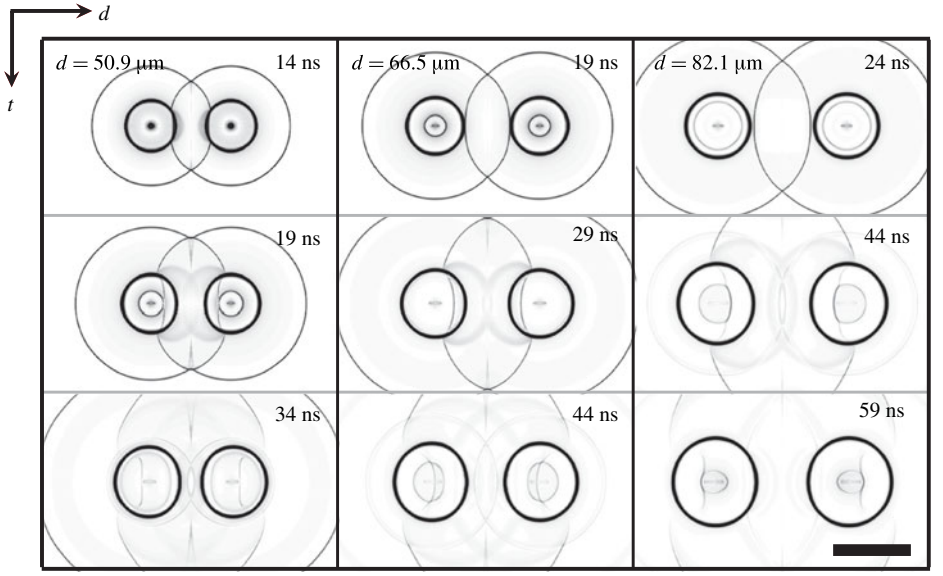



FIGURE 3. Simulation (Schlieren) for cases shown in figure 2 between dashed lines with $R_0 = 8$ μm and $P_i = 2$ GPa. The length of the scale bar is 50 μm.

The probability for bubble nucleation as a function of separation is shown in figure 4(*b*). The data show a monotonic decrease in the probability as $d$ increases.

Simulations show that the lowest pressures are reached at the contact plane at $(x, y) = (0, 0)$ due to the overlap of the tensions. Evolution of the pressure at $(0, 0)$ is shown in figure 4(*c*) for each $d$. The liquid is exposed to negative pressure for a time of 3–17 ns (figure 4*c*, inset). The lowest values of the calculated pressures $P_{min}$ are plotted as a function of $d$ in figure 4(*d*). The overall trend is a monotonic increase of the pressure with $d$, with the exception of the two smallest and largest values of $d$. The minimum pressures for the two smallest separations are essentially the same, −27.8 and −27.5 MPa for $d = 50.9$ and $d = 58.8$ μm, respectively. Yet, for the smallest $d$ the probability of cavitation is maximum (0.92). The very small pressure change at the smallest separation can be explained by the continuous destructive interference of the reflected tensions with stronger shocks, decreasing the change in tension for the shortest distance. For the two largest separations (97.9 and 106.8 μm), the general trend reverses and the minimum pressure decreases (for $d = 106.8$ μm), in contrast to the experimental measurements, where the probability for nucleation decreases monotonically with $d$ (figure 4*b*). The change in the minimum pressure might be partly explained by the model, which assumes an ideal gas inside the laser-induced bubbles (Aitken, McCluskey & Denat 1996). The assumption tends to be invalid at later times when the bubble expansion rate decreases and evaporation effects on the bubble dynamics become more important, making the solution less accurate as $d$ increases.

The discrepancies in the measured probabilities (figure 4*b*) and the minimum pressures predicted by the model (figure 4*d*) could be explained by a temperature



https://doi.org/10.1017/jfm.2013.456 Published online by Cambridge University Press

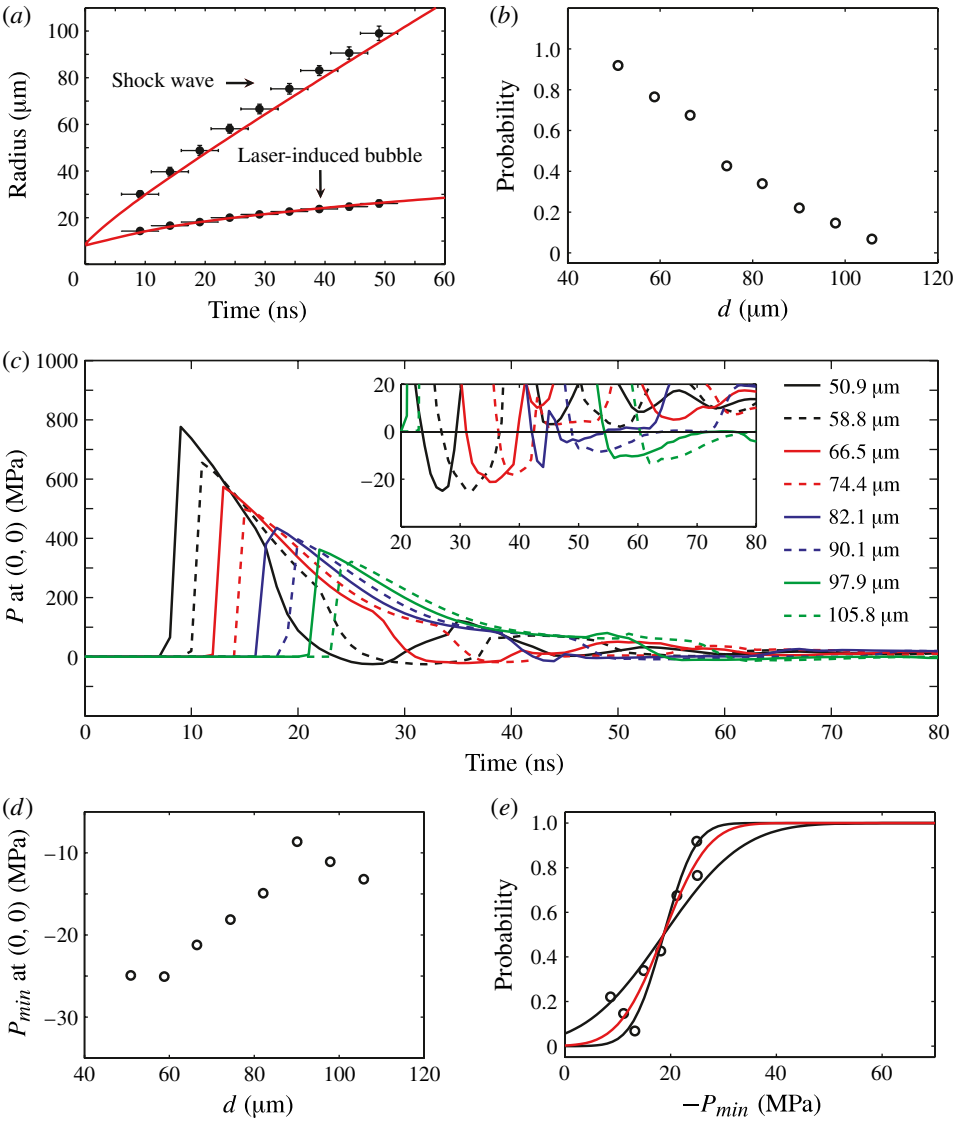



FIGURE 4. (*a*) Dynamics of individual bubbles and shocks produced by a single plasma (72.5 μJ at each focal volume). (*b*) Probability of cavitation inception as a function of separation $d$. (*c*) Pressure at $(x, y) = (0, 0)$ as a function of time for the eight distances. (*d*) Minimum pressure attained at $(x, y) = (0, 0)$. (*e*) Probability of cavitation inception as a function of calculated minimum pressure. Continuous red line (centre) is the fit to the error function, $a = 0.105 \pm 0.045$ MPa$^{-1}$ and $P_{th} = -18.7 \pm 2$ MPa. The black lines represent the errors due to the slope $a$.

rise with decreasing $d$. The energy barrier for nucleation decreases with temperature, and hence nucleation would be more likely for the shortest $d$, even at the same pressure.

A process that could raise the temperature is an adiabatic compression during the initial overlap of the shock waves. However, an adiabatic process should follow the



https://doi.org/10.1017/jfm.2013.456 Published online by Cambridge University Press

shape of the pressure wave (figure 4*c*); the end result would be a slight decrease in temperature (fraction of a degree) during the negative pressure cycle. Hence, if the thermodynamic processes are adiabatic, these should not make a significant difference in the temperature.

Figure 4(*d*) shows the measured probability for bubble nucleation as a function of the calculated absolute value of the minimum pressure ($-P_{min}$). All the data are fitted to an error function $0.5[1 + \mathrm{erf}(a(P - P_{th}))]$ or *s*-curve, where $a$ is the sharpness or the slope and $P_{th}$ is the threshold pressure where the probability of bubble nucleation is one-half. The fit yields $a = 0.105 \pm 0.045$ MPa$^{-1}$ and $P_{th} = -18.7 \pm 2$ MPa.

We repeated the experiment using a larger laser energy of 84.9 μJ per focus; the fitted initial conditions for the plasma are $R_0 = 8$ μm and $P_i = 2.5$ GPa. The data are shown in figure 5. The dynamics of the measured individual shocks and bubbles are shown in figure 5(*a*), where each data point represents 80 events (left, right, eight separations, five repetitions). The probability of bubble nucleation is measured at each $d$ for 129–151 events. Figure 5(*b*) shows the probability for bubble nucleation as a function of $d$; the probability decreases monotonically with $d$. The pressure evolution for the system of two plasmas predicted by the numerical simulation at $(0, 0)$ is shown in figure 5(*c*) for all the separations. The minimum pressures $P_{min}$ achieved at each $d$ are plotted in figure 5(*d*). We observe a similar trend to that for the 2 GPa data (figure 4*d*); in this case the minimum pressure for the shortest separation $P_{min} = -35.3$ MPa ($d = 50.9$ μm) is slightly higher than the pressure at a separation of 58.9 μm (−36.2 MPa). Figure 5(*e*) shows the measured probability for bubble nucleation as a function of the calculated absolute value of the minimum pressure ($-P_{min}$). The extracted threshold pressure is $P_{th} = -20.9 \pm 2.6$ MPa, and $a = 0.075 \pm 0.028$ MPa$^{-1}$. The threshold pressures for both experiments are inside the interval $P_{th} = -20.1 \pm 3.4$ MPa. Our results are repeatable for experiments with different initial conditions. However, as in most acoustic experiments, our results disagree with the predictions of classical nucleation theory for homogeneous nucleation, probably because of unidentified impurities that are common to all experiments that use dynamic stretching techniques regardless of preparation of the water sample. It has been proposed that the impurities are stable nanobubbles or nanonuclei (Sankin & Teslenko 2003; Bunkin *et al.* 2009; Weijs, Seddon & Lohse 2012; Bunkin & Bunkin 2013; Maxwell *et al.* 2013).

## 6. Discussion

In this section we discuss the discrepancies between this experiment and other acoustic experiments. Classical nucleation theory considers the volume $V$ exposed to tension as well as its duration $\tau$. Thus, the homogeneous cavitation pressure depends on the product $V\tau$, as explained in Herbert, Balibar & Caupin (2006). In our experiment, $\tau \sim 10$ ns and the probed volume has a characteristic dimension smaller than 20 μm. Table 1 summarizes the results of the experiments that are used to compare with this work. We start by comparing our results with an experiment with similar spatial and temporal scales in water saturated with ambient gas (Ando *et al.* 2012). Hence, according to the theory, the expected cavitation inception pressure should be similar. However, the definition of the threshold cavitation pressure is different (i.e. individual versus statistical). In that experiment, a single laser-induced shock reflects at a straight air–water interface inside a microfluidic channel as a focusing tension. The nucleated bubble clouds were observed with certainty (probability = 1), and the reported threshold pressure of $-60 \pm 5$ MPa



https://doi.org/10.1017/jfm.2013.456 Published online by Cambridge University Press

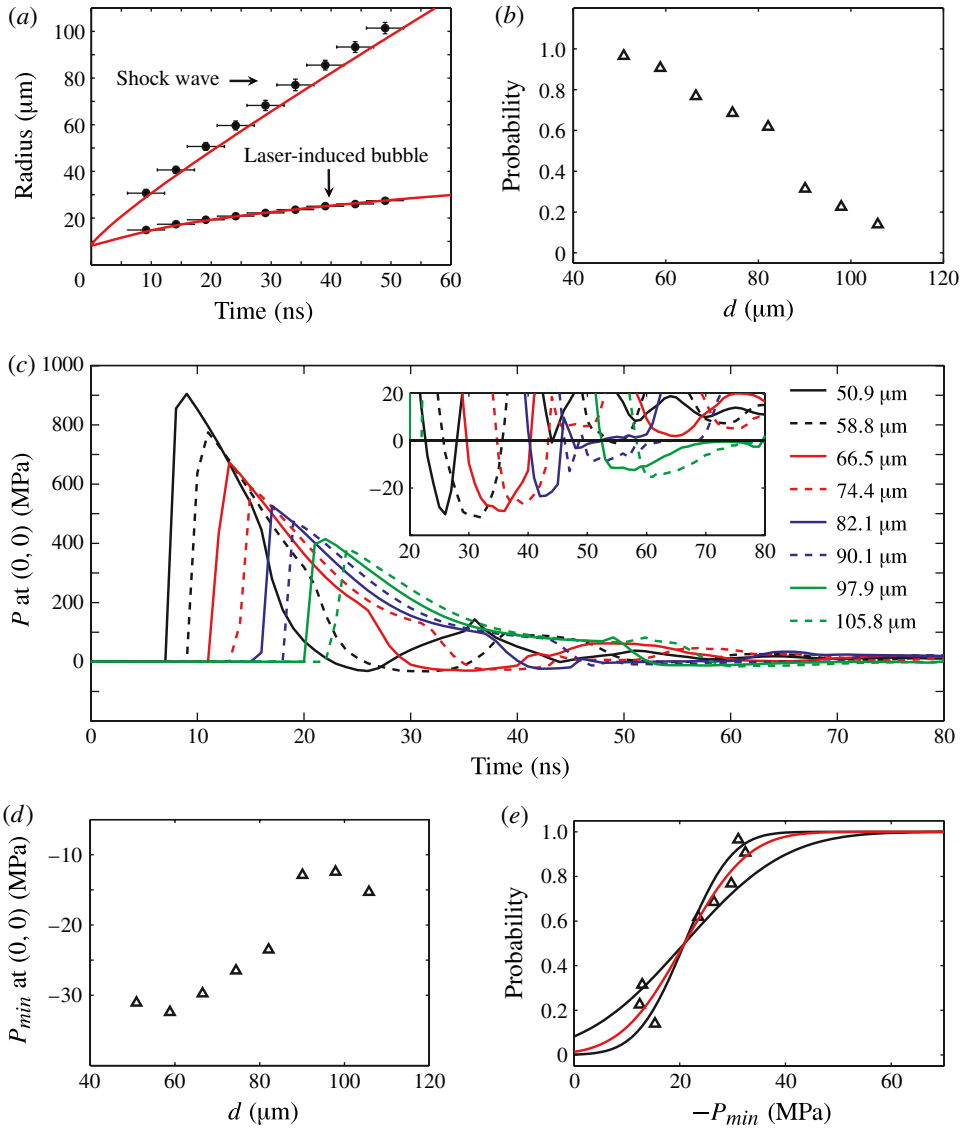



FIGURE 5. (*a*) Dynamics of individual bubbles and shocks produced by a single plasma (84.9 μJ at each focal volume). (*b*) Probability of cavitation inception as a function of separation $d$. (*c*) Pressure at $(x, y) = (0, 0)$ as a function of time for the eight distances. (*d*) Minimum pressure attained at $(x, y) = (0, 0)$. (*e*) Probability of cavitation inception as a function of calculated minimum pressure. Continuous red line (centre) is the fit to the error function: $a = 0.075 \pm 0.028\ \mathrm{MPa}^{-1}$ and $P_{th} = -20.9 \pm 2.6$ MPa. The black lines represent the errors due to the slope $a$.

relied on individual events and the location of the bubble cloud, in contrast to the statistical approach of this work. To compare with this work, we look at the cavitation inception pressure at a probability close to unity. Figures 4(*e*) and 5(*e*) show that, only considering the errors on the slope of the fitted *s*-curves (black continuous lines), the absolute value of the pressure at a probability of 0.98 lies in the interval (28, 43) MPa



https://doi.org/10.1017/jfm.2013.456 Published online by Cambridge University Press

| Water sample | Method | $\tau$ | $P_{th}$ definition | $P_{th}$ (MPa) | Reference |
|---|---|---|---|---|---|
| Gas saturated | Reflected shock | 5 ns | Individual | $-60 \pm 5$ | Ando *et al.* (2012) |
| Degassed | Focused ultrasound | $1/f = 0.5$ μs | Statistical | $-30$ | Arvengas *et al.* (2011) |
| 10 % $O_2$ | Focused ultrasound | $1/f = 0.9$ μs | Statistical | $(-28.1, -26.9)$ | Maxwell *et al.* (2013) |
| 90 % $O_2$ | Focused ultrasound | $1/f = 0.9$ μs | Statistical | $(-26.4, -26)$ | Maxwell *et al.* (2013) |
| Gas saturated | Reflected shock | 3–17 ns | Statistical | $-20.1 \pm 3.4$ | This work |

TABLE 1. Measured values of $P_{th}$ for water at room temperature. Here $\tau$ is the duration of the negative pressure cycle and $f$ is the ultrasound frequency.

for the 2 GPa data and (35, 52) MPa in the case for the plasmas with $P_i = 2.5$ GPa. The tensions predicted by our fitted $s$-curves are consistent with the observations made in the microfluidic experiment of Ando *et al.* (2012) for a probability close to unity.

Next, we compare our results with other ultrasound experiments with larger $V\tau$, where the duration of the negative pressure cycle $\tau \sim 1$ μs and the dimensions of the focal region have a length scale of the order of a millimetre. Contrary to the theoretical prediction, our measured cavitation threshold pressure is less negative. This suggests the existence of impurities that cannot be optically detected by our imaging system (spatial resolution of hundreds of nanometres). An experiment with focused ultrasound bursts at 1 and 2 MHz in degassed and pre-pressurized water (Arvengas, Davitt & Caupin 2011) achieves slightly lower pressure thresholds for cavitation inception with ultrasound at 2 MHz ($\sim -30$ MPa at 20 °C), which is more negative than the threshold reported in this work. Recently, it has been shown by Maxwell *et al.* (2013) that the threshold for bubble nucleation depends on the gas concentration. In their experiment, they used a two-cycle ultrasound burst at 1.1 MHz. They observed that the statistical cavitation inception threshold (probability of 0.5) depends on the gas content of the water sample. For distilled degassed (10 % $O_2$ concentration) water samples, they measured a threshold between $-26.9$ and $-28.1$ MPa at room temperature, while for mildly degassed (90 % $O_2$ concentration) unfiltered tap water the threshold varied between $-26.0$ and $-26.4$ MPa. Using the measured pressure thresholds ($\sim -28$ MPa) and classical Rayleigh–Plesset calculations, they estimate the radius of (stabilized) cavitation nuclei $r_0 \sim 2.5$ nm that expand to visible sizes ($10^4 r_0$) at minimum pressures starting at the threshold value. The estimated nanocavity radius of 2.5 nm is much smaller than the resonant radius at 1.1 MHz. As a result, their simulated cavitation threshold is essentially independent of the ultrasound frequency in the range between 0.1 and 10 MHz. Nanonuclei contaminants with similar dimensions were calculated by Sankin & Teslenko (2003) and by molecular dynamics simulations of Weijs *et al.* (2012), showing that nanobubble clusters can be thermodynamically stable.



https://doi.org/10.1017/jfm.2013.456 Published online by Cambridge University Press

In our experiment with ultrapure water saturated with ambient gas, the measured pressure threshold for cavitation ($-20.1 \pm 3.4$ MPa) is less negative than that of the mildly degassed sample ($\sim -26$ MPa) in Maxwell *et al.* (2013), which suggests the presence of more gas contaminants ($<0.5$ μm, thus not detected by the imaging system). Furthermore, the slope of our fitted *s*-curves is significantly smaller than those in the ultrasound experiments mentioned above. That is, in those experiments they reach a probability of unity at a pressure of 1–2 MPa below the reported thresholds. In contrast, for our experiments we measure a probability approaching unity ($>0.9$) at $\sim$10 MPa below the threshold. This suggests the presence of nanonuclei contaminants with a wide size distribution that expand to visible sizes at pressures starting at different minimum values. Dicker *et al.* (2010) measured the probability of destruction of bubble shells as a function of pressure, and showed that the slope of their *s*-curves is shallower for polydisperse samples. Light scattering measurements (Bunkin *et al.* 2009) on doubly distilled water were fitted to polydisperse bubble distributions, with means in the range of tens of nanometres. We believe that in our experiment the extra gas impurities come from the process of laser-induced cavitation. These contaminants should be added by the bubble remnants left after the collapse of the laser-induced bubbles. During each experiment, the laser-induced bubbles were created continuously every five seconds, and therefore the concentration of gas nuclei should reach an equilibrium after several laser-induced cavitation events, raising the pressure threshold for cavitation.

## 7. Conclusions

We have shown that it is possible to nucleate bubble clouds due to the interaction between a pair of laser-induced shocks and bubbles. The statistical pressure threshold for cavitation inception of $-20.1 \pm 3.4$ MPa is less negative than the value reported in other acoustic experiments, probably due to gas nanonuclei contaminants originating from the laser-induced bubble remnants. The results should be relevant to applications that use multiple laser-induced bubbles and particularly those created with optical breakdown, since most applications do not consider the possibility of generating strong tensions.

Future work will include the effect of the shocks on the dynamics of the laser-induced bubbles (Sankin *et al.* 2005) and instabilities at the surfaces of the bubbles (Layes *et al.* 2003; Chu & Chen 2013).

## Acknowledgements

P.A.Q.-S. thanks A. U'Ren and P. Carreón for sharing laboratory space and for the ultrapure water system. He acknowledges financial support from CONACYT (project 153821) and DGAPA, UNAM (project PAPIIT-TB100312). K.A. acknowledges support by JSPS KAKENHI Grant Number 25709008.

## Supplementary material

Supplementary material is available at http://dx.doi.org/10.1017/jfm.2013.456.

## References

AITKEN, F., MCCLUSKEY, F. M. J. & DENAT, A. 1996 An energy model for artificially generated bubbles in liquids. *J. Fluid Mech.* **327**, 373–392.



https://doi.org/10.1017/jfm.2013.456 Published online by Cambridge University Press

ANDO, K., LIU, A. Q. & OHL, C. D. 2012 Homogeneous nucleation in water in microfluidic channels. *Phys. Rev. Lett.* **109**, 044501.

ARVENGAS, A., DAVITT, K. & CAUPIN, F. 2011 Fiber optic probe hydrophone for the study of acoustic cavitation in water. *Rev. Sci. Instrum.* **82**, 034904.

BUNKIN, N. F. & BUNKIN, F. V. 2013 Bubston structure of water and aqueous solutions of electrolytes. *Phys. Wave Phenom.* **21**, 81–109.

BUNKIN, N. F., SUYAZOV, N. V., SHKIRIN, A. V., IGNATIEV, P. S. & INDUKAEV, K. V. 2009 Nanoscale structure of dissolved air bubbles in water as studied by measuring the elements of the scattering matrix. *J. Chem. Phys* **130**, 134308.

CHU, H. Y. & CHEN, D. K. 2013 Observations of three-dimensional Richtmyer–Meshkov instability on a membraneless gas bubble. *Phys. Rev.* E **87**, 051002.

DICKER, S., MLECZKO, M., SCHMITZ, G. & WRENN, S. P. 2010 Determination of microbubble cavitation threshold pressure as function of shell chemistry. *Bubble Sci. Eng. Technol.* **2**, 55–64.

GERCHBERG, R. W. & SAXTON, W. O. 1972 A practical algorithm for the determination of the phase from image and diffraction plane pictures. *Optik* **35**, 237–246.

HAAS, J. F. & STURTEVANT, B. 1987 Interaction of weak shock waves with cylindrical and spherical gas inhomogeneities. *J. Fluid Mech.* **181**, 41–76.

HERBERT, E., BALIBAR, S. & CAUPIN, F. 2006 Cavitation pressure in water. *Phys. Rev.* E **74**, 041603.

JAYASINGHE, A. K., ROHNER, J. & HUTSON, M. S. 2011 Holographic UV laser microsurgery. *Biomed. Opt. Express* **2**, 2590–2599.

JOHNSEN, E. & COLONIUS, T. 2006 Implementation of WENO schemes in compressible multicomponent flow problems. *J. Comput. Phys.* **219**, 715–732.

JOHNSEN, E. & COLONIUS, T. 2009 Numerical simulations of non-spherical bubble collapse. *J. Fluid Mech.* **629**, 231–262.

LAYES, G., JOURDAN, G. & HOUAS, L. 2003 Distortion of a spherical gaseous interface accelerated by a plane shock wave. *Phys. Rev. Lett.* **91**, 174502.

LEIGHTON, T. G. 1994 *The Acoustic Bubble*. Academic Press.

MAXWELL, A. D., CAIN, C. A., HALL, T. L., FOWLKES, J. B. & XU, Z. 2013 Probability of cavitation for single ultrasound pulses applied to tissues and tissue-mimicking materials. *Ultrasound Med. Biol.* **39**, 449–465.

MAXWELL, A. D., WANG, T. Y., CAIN, A., FOWLKES, J. B., SAPOZHNIKOV, O. A., BAILEY, M. R. & XU, Z. 2011 Cavitation clouds created by shock scattering from bubbles during histotripsy. *J. Acoust. Soc. Am.* **130**, 1888–1898.

OHL, C. D. & OHL, S. W. 2013 *Bubble Dynamics and Shock Waves*, pp. 3–31. Springer.

QUINTO-SU, P. A., HUANG, X. H., GONZALEZ-AVILA, S. R., WU, T. & OHL, C. D. 2010 Manipulation and microrheology of carbon nanotubes with laser-induced cavitation bubbles. *Phys. Rev. Lett.* **104**, 014501.

QUINTO-SU, P. A. & OHL, C. D. 2009 Interaction between two laser-induced cavitation bubbles in a quasi-two-dimensional geometry. *J. Fluid Mech.* **633**, 425–435.

RANJAN, D., OAKLEY, J. & BONAZZA, R. 2011 Shock–bubble interactions. *Annu. Rev. Fluid Mech.* **43**, 117–149.

SANKIN, G. N. & TESLENKO, V. S. 2003 Two-threshold cavitation regime. *Dokl. Phys.* **48**, 665–668.

SANKIN, G. N., SIMMONS, W. N., ZHU, S. L. & ZHONG, P. 2005 Shock wave interaction with laser-generated single bubbles. *Phys. Rev. Lett.* **95**, 034501.

SANKIN, G. N., YUAN, F. & ZHONG, P. 2010 Pulsating tandem microbubble for localized and directional single-cell membrane poration. *Phys. Rev. Lett.* **105**, 078101.

WEIJS, J. H., SEDDON, J. R. T. & LOHSE, D. 2012 Diffusive shielding stabilizes bulk nanobubble clusters. *Chem. Phys. Chem.* **13**, 2197–2204.

https://doi.org/10.1017/jfm.2013.456 Published online by Cambridge University Press